Statistical properties of fractal type dislocation cell structures

Sándor Lipcsei [1], Szilvia Kalácska [2,3], Péter Dusán Ispánovity [1,4], János L. Lábár [5],
Zoltán Dankházi [1], and István Groma [1,*]

[1]*Eötvös Loránd University, Department of Materials Physics, 1117 Budapest, Pázmány Péter Sétány 1/a, Hungary*
[2]*Mines Saint-Etienne, Univ. Lyon, CNRS, UMR 5307 LGF, Centre SMS, 158 Cours Fauriel, 42023 Saint-Étienne, France*
[3]*Empa, Swiss Federal Laboratories for Materials Science and Technology, Laboratory of Mechanics of Materials and Nanostructures,
CH-3602 Thun, Feuerwerkerstrasse 39, Switzerland*
[4]*Institute for Advanced Simulation: Materials Data Science and Informatics (IAS-9),
Forschungszentrum Jülich GmbH, 52425 Jülich, Germany*
[5]*Thin Film Physics Department, Institute of Technical Physics and Materials Science, Centre for Energy Research, 1121 Budapest, Konkoly
Thege M. u. 29-33, Hungary*

The dislocation microstructure developing during plastic deformation strongly influences the stress-strain properties of crystalline materials. Resent theoretical investigations based on the 2D continuum theory of straight parallel edge dislocations were able to predict a periodic dislocation microstructure. The results obtained, however, can only be considered as a very first step toward the understanding of the origin of dislocation patterning. One of the most challenging problems is the modeling of the formation of the fractal like dislocation microstructure. So, it is crucial to determine the statistical properties of such a structure developing at ideal multiple slip orientation. In the paper, by x-ray line profile analysis and the method of high resolution electron backscatter diffraction (HR-EBSD) a complex experimental characterization of dislocation microstructure developing in uniaxially compressed Cu single crystals is presented. With these methods, the maps of the internal stress, the Nye tensor, and the geometrically necessary dislocation (GND) density were determined at different load levels. It is found from the fractal analysis of the GND maps that the fractal dimension of the cell structure is decreasing with increasing average spatial dislocation density fluctuation. Moreover, it is shown that the evolution of different types of dislocations can be successfully monitored with the HR-EBSD-based technique.

I. INTRODUCTION

It was first observed nearly 60 years ago that dislocations created during the plastic deformation of crystalline materials tend to form different patterns with the morphology depending on the mode, temperature, and rate of deformation. There is an equally longstanding discussion regarding the physical origin of these patterns. A large variety of approaches have been proposed to model the instability leading to the spatial variation of the dislocation density, many of which are based upon analogies with pattern formation in other physical systems. It has been argued that dislocation patterns can be understood by the tendency toward the minimization of some kind of elastic energy functional (Hansen and Kuhlmann-Wilsdorf [1], Holt [2], Rickman and Vinas [3]), but the theories have never been worked out in detail. Another approach proposed is to model the dislocation patterning as a reaction-diffusion phenomenon of the mobile and immobile dislocation densities (Walgraef and Aifantis [4], Pontès *et al.* [5]). The fundamental problem with this approach is that it is completely phenomenological, i.e., one cannot see how the different terms appearing in the evolution equations are related to the properties of individual dislocations.

In a recent series of papers [6–8], a theoretical approach based on a continuum theory of dislocations, derived from the evolution of individual dislocations, was proposed for modeling the patterning process. According to the theory, the main source of the instability is the nontrivial mobility of the dislocations caused by the finite flow stress, while the characteristic length scale of the pattern is selected by diffusionlike terms appearing in the theory due to dislocation correlation effects. Since, however, the theory is developed for a rather idealized 2D dislocation configuration, further experimental and theoretical investigations are needed to create a general comprehensive theory of dislocation patterning.

One of the most challenging issues is the characterization and modeling of the self-similar fractal-like dislocation cell structure formed in face-centered cubic (FCC) crystals oriented for ideal multiple slip (for details, see the pioneering works of Zaiser and Hähner [9,10]). For developing an appropriate theory of the problem, one should determine experimentally the statistical properties of the fractal-like dislocation microstructures. Since copper single crystal is an easily processable model material, this paper reports on detailed experimental investigations performed on compressed Cu single crystals oriented for ideal multiple slip. To get a complex picture of the dislocation cell structure, as a first step, the earlier investigations performed by x-ray line profile analysis (XPA) and TEM investigations on samples compressed

---

*Corresponding author: groma@metal.elte.hu

up to different stress levels (Székely *et al.* [11]) were revisited. It should be noted that with the x-ray detectors available nowadays, one can achieve a much better signal-to-noise ratio than previously. This improves considerably the accuracy of the parameters obtained from the x-ray profiles. Moreover, as a relatively recently developed method, high-angular resolution electron backscatter diffraction (HR-EBSD) investigations were also performed on the samples. With this, the maps of the internal stress and the geometrically necessary dislocation (GND) density developing in the samples could be determined. Some of the aspects of the applied methods are developed exclusively for the specific requirements of the addressed problem; consequently, in the first half of the paper the applied experimental methods are explained in detail. In the second part, the obtained experimental results are discussed. The obtained statistical results (e.g., fractal dimension) have been confirmed by the simulations done by Bakó and Hoffelner [12], which predict the formation of dislocation cell structures with nontrivial fractal dimension in the absence of climb for multiple slip oriented FCC materials. Nevertheless, the earlier TEM observations, courtesy of Essmann in the work of Hähner and Zaiser [13], on uniaxially deformed copper single crystals validate many of our results regarding the statistical parameters.

II. EXPERIMENTAL METHODS

A. Sample preparation

To study the dislocation cell formation mechanism in FCC materials, a high-purity copper single crystal was used. For the compression tests, rectangular prism-shaped samples with dimensions of $2.5 \times 2.5 \times 5$ mm^3 were cut with an electrical discharge machine (EDM). The orientation of each surface was of the (100) type. For removing the amorphous layer created by EDM, the specimens were etched in a 30% HNO$_3$ solution for 10 min. To reduce the initial dislocation density, the samples were heat treated at 600 °C for 6 h in a vacuum furnace. The average dislocation density in an undeformed sample was determined by XPA (the details of the method applied are explained below in Sec. II B). It was found that it is below the 1×10^{13} m^{-2} lower limit that one can determine by x-ray profile analysis.

The samples were compressed from the direction of the square-shaped surfaces, ensuring uniaxial deformation in the [001] direction corresponding to ideal multiple slip. The EBSD and XPA measurements were performed on the [010] surface.

Six different samples with the same size and orientation were deformed up to different strain levels. The resolved shear stress τ^* versus strain ε curve of the sample with the highest terminal deformation is shown in Fig. 1. The black dots on the curve mark the maximum stresses and strain levels of the six different samples. (Up to the maximum stress levels, the stress-strain curves obtained on the other samples follow the same curve as the one plotted within 5% of error.) The black line in the figure shows the hardening rate $\Theta = d\tau/d\varepsilon$ as a function of strain. As expected for ideal multiple slip [14], the $\Theta(\varepsilon)$ curve consists of a nearly
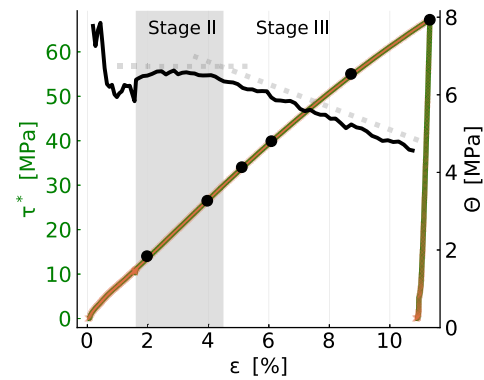

FIG. 1. Resolved shear stress (τ^*) and hardening rate (Θ) versus strain (ε) obtained on a compressed Cu single crystal oriented for (001) ideal multiple slip. The black dots on the curve mark the stress levels until which the six different samples were compressed.

horizontal (stage II) and decreasing (stage III) linear part. This is indicated by the dotted lines in the figure.

From the six specimens prepared, three are close to the strain level corresponding to the transition from stage II to stage III. As seen below, this strain region is critical for the statistical properties of the dislocation cell structure developing during the deformation.

Finally, to prepare the samples for TEM and HR-EBSD measurements, electropolishing was applied at 20 V, 1.2 A using Struers D2 electrolyte for 30 s.

B. X-ray line profile analysis

XPS is a well-established method to determine the average dislocation density, the average squared dislocation density, and the dislocation polarization from the measured intensity profile. In our analysis, the "restricted moments" method developed by Groma *et al.* [15–17] was applied. In the evaluation of the measured data the asymptotic behavior of the different order restricted moments are analyzed. The kth order restricted moments are defined as

$$v_k(q) = \frac{\int_{-q}^{q} q'^k I(q') dq'}{\int_{-\infty}^{\infty} I(q') dq'}, \tag{1}$$

where q is the varying integration limit the restricted moment $v_k(q)$ depends on; $I(q')$ is the intensity distribution near to a Bragg peak, in which $q' = 2(\sin\theta - \sin\theta_0)/\lambda$; λ is the wavelength of the applied x rays, and θ and θ_0 are the half of the diffraction and Bragg angles, respectively.

As explained in detail in Ref. [15], for large enough q values the asymptotic form of the second order restricted moment reads

$$v_2(q) = 2\Lambda \langle \rho \rangle \ln\left(\frac{q}{q_0}\right), \tag{2}$$

where $\langle \rho \rangle$ is the average dislocation density, q_0 is a parameter determined by the dislocation-dislocation correlation, and Λ is a constant depending on the dislocation Burgers vector $\vec{b}$, the line direction $\vec{l}$, and the diffraction vector $\vec{g}$. Λ is commonly written in the form $\Lambda = \pi |\vec{g}|^2 |\vec{b}^2| C/2$ where C is called the contrast factor. (For its actual value, a detailed

deduction and explanation can be found in Ref. [15].) From the intensity profiles measured, the values of $\Lambda\langle\rho\rangle$ and q_0 can be obtained by fitting a straight line on the asymptotic part of the $v_2(q)$ versus $\ln(q)$ plot. It should be noted that if the dislocation density is less than about 10^{13} m^{-2}, the instrumental broadening is in the same order as the one caused by the dislocations, so dislocation density below this limit cannot be accurately determined by the x-ray profile analysis performed in a laboratory setup applied in the investigations.

Besides the second-order restricted moment for our analysis, the fourth-order restricted moment is also important. In the asymptotic regime, it is [15]

$$v_4(q) = \Lambda\langle\rho\rangle q^2 + 12\Lambda^2\langle\rho^2\rangle \ln^2\left(\frac{q}{q_1}\right), \qquad (3)$$

where $\langle\rho^2\rangle$ is the average dislocation density fluctuation, and q_1 is a parameter. For better visualization, it is useful to consider the quantity

$$\frac{v_4(q)}{q^2} = \Lambda\langle\rho\rangle + 12\Lambda^2\langle\rho^2\rangle \frac{\ln^2\left(\frac{q}{q_1}\right)}{q^2}, \qquad (4)$$

which asymptotically tends to $\Lambda\langle\rho\rangle$. The actual values of the parameters $\Lambda\langle\rho\rangle$, $\Lambda^2\langle\rho^2\rangle$, and q_1 can be determined by fitting the form given by Eq. (4) to the asymptotic regime of the $v_4(q)/q^2$ versus q plot.

An important statistical parameter of the dislocation microstructure developed is the relative dislocation fluctuation defined as

$$\sigma = \sqrt{\frac{\langle\rho^2\rangle - \langle\rho\rangle^2}{\langle\rho\rangle^2}}, \qquad (5)$$

which can be determined from the fourth-order restricted moment.

It should be noted that the measured intensity $I(q')$ often contains a background which has to be subtracted before the calculation of the restricted moments. Since, however, the background has different contributions to the second- and fourth-order restricted moments, determining the average dislocation density from both moments offers a internal checking possibility whether the background level was selected correctly.

The profile measurements have been performed with a Cu rotating anode Cu x-ray generator at 40 kV and 100 mA with wavelength $\lambda = 0.15406$ nm. To reduce the instrumental broadening, the symmetrical (220) reflection of a Ge monochromator was used. The Kα_2 component of the Cu radiation was eliminated by an 0.1 mm slit between the source and the Ge crystal. The profiles were registered by a linear position sensitive DECTRIS MYTHEN2 R detector with 50 μm spatial resolution and 1280 channels. The sample-detector distance was 0.7 m, resulting in an angular resolution on the order of 0.004°. During the measurements, approx. 1x1 mm^2 surfaces of the samples were illuminated by the x ray, so the parameters obtained from x-ray measurements correspond to average values over areas much larger than the typical dislocation cell size (see below).

The evaluation method applied is demonstrated on the intensity distribution (Fig. 2) obtained on the sample com-
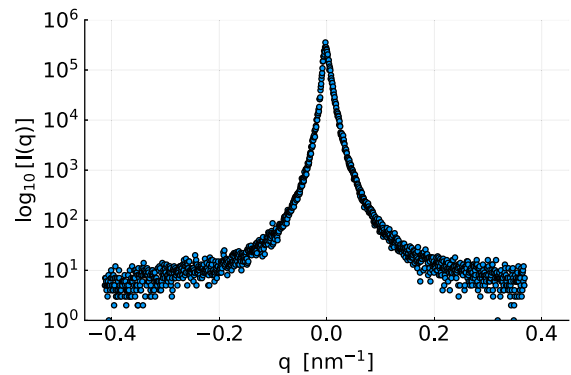

FIG. 2. The x-ray line profile obtained at $\vec{g} = (020)$ on the sample compressed up to 43.12 MPa. To eliminate the effect of the noise, the peak intensity should be at least $10^3 - 10^4$ times higher than the background, and a subsequent background subtraction should be carried out.

pressed up to 43.12 MPa resolved shear stress. The corresponding restricted moments are shown in Fig. 3. As shown in the figure, the different parameters can be determined with an accuracy of less than a few percent.

C. HR-EBSD

EBSD measurements were carried out in a FEI Quanta 3D scanning electron microscope (SEM) equipped with an Edax Hikari EBSD detector. Diffraction patterns were recorded with 1×1 binning (640 px $\times$ 480 px resolution) using an electron beam of 20 kV, 16 nA. To carry out statistical analysis on the collected data, a 20 μm $\times$ 20 μm area was mapped with a step size of 100 nm on each sample. The HR-EBSD technique utilizes image cross-correlation on the recorded diffraction patterns [18]. The local strain tensor components can be determined, and a lower bound estimate of the GND density can be given using the commercially
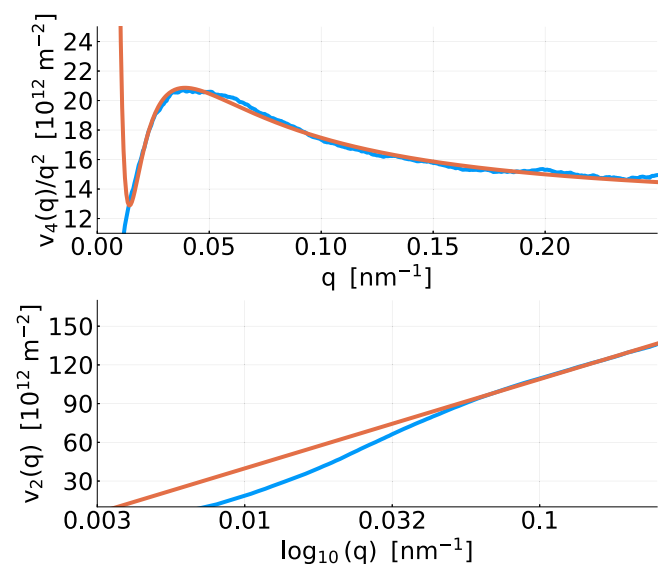

FIG. 3. The raw data (blue lines) and the fitted restricted moments (orange lines).

available software. The method requires an ideally stress-free diffraction pattern as reference that is often difficult to obtain experimentally. In the absence of such reference, it is noted that the scales should be implemented as relative and not absolute measures. Image cross-correlation based HR-EBSD calculations were performed using BLG Vantage CrossCourt v.4 software that provided the components of the elastic distortion (β_{ij}^{el}) and the stress tensor (σ_{ij}) and the also the values of the GND density (ρ_{GND}).

From the distortion map, the Nye dislocation density tensor α_{ij}, defined as [19]

$$\alpha_{ij} = -e_{klj}\partial_k\beta_{il}^{\text{el}}, \tag{6}$$

can also be determined, where e_{ijk} is the Levi-Civita symbol. Since, however, in the HR-EBSD measurement the distortion tensor is measured directly on the sample surface, only those components of α_{ij} can be calculated that are independent from the derivation in the direction perpendicular to the sample surface. So, in a coordinate system with the z axis perpendicular to the sample surface, only the iz components of the Nye tensor

$$\alpha_{iz} = \partial_y\beta_{ix}^{\text{el}} - \partial_x\beta_{iy}^{\text{el}} \quad i = x, y, z \tag{7}$$

can be directly determined from a HR-EBSD measurement. With some additional assumptions, one can determine further components of the α_{ij} tensor [20] but, since to see the validity of the assumptions required is not straightforward, only the α_{iz} were used in the investigations presented.

Since

$$\alpha_{ij} = \sum_t b_i^t l_j^t \rho^t, \tag{8}$$

where the superscript t denotes a given type of dislocation present in the system with Burgers vector $\vec{b}^t$, line direction $\vec{l}^t$, and dislocation density ρ^t, from the measured Nye tensor components, one can make an estimate on the dislocation population in the different slip systems (for details see below).

Furthermore, to characterize the GND density, the scalar quantity

$$\rho_{\text{GND}} = \frac{1}{b}\sqrt{\alpha_{xz}^2 + \alpha_{yz}^2 + \alpha_{zz}^2} \tag{9}$$

was introduced. The GND density and the α_{iz} tensor components were determined using a C + + code developed by some of the authors [21,22].

III. STRESS-MAP ANALYSIS WITH THE RESTRICTED MOMENT METHOD

It was already demonstrated earlier by Groma and Bakó, Csikor and Groma, and Wallis *et al.* [23–25] that for a dislocation ensemble of parallel edge dislocations the asymptotic part of the probability distribution of the internal stress $p(\sigma)$ decays as

$$p(\sigma) \approx \frac{b^2\mu^2}{8\pi^2}C\langle\rho\rangle\frac{1}{\sigma^3}, \tag{10}$$

where μ is the shear modulus and C is a geometrical constant, similar to the contrast factor in the case of x-ray peaks, depending on the type of dislocation, the normal direction of that
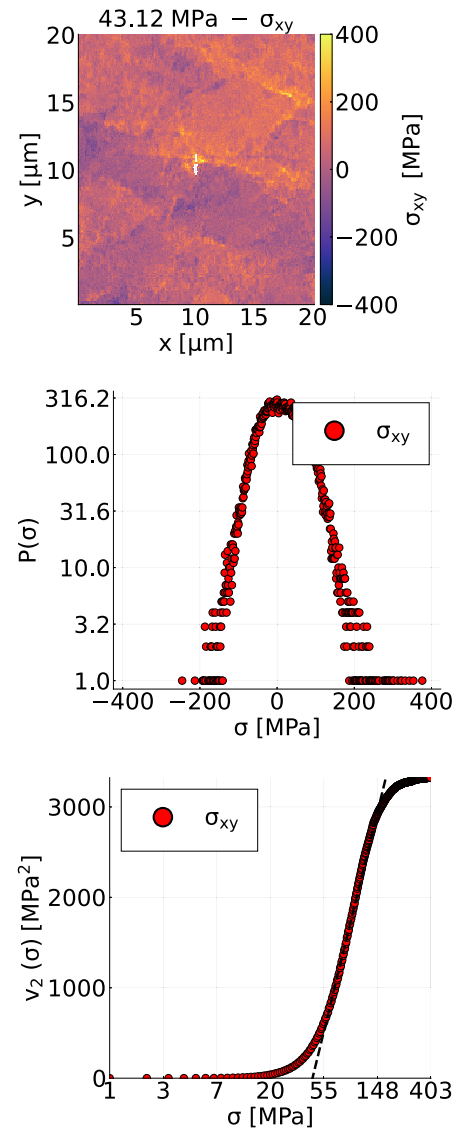

FIG. 4. Stress map, stress probability distribution, and the corresponding second order restricted moment v_2 versus $\ln(\sigma)$ obtained on the sample compressed up to 43.12 MPa.

surface of the sample, on which the measurements are carried out, and the stress component σ considered. So, like for x-ray line broadening, in the asymptotic regime the second-order restricted moment $v_2(\sigma)$ is linear in $\ln(\sigma)$. From its slope, one can determine the quantity $\rho^* = C < \rho >$, often referred to as formal dislocation density. It should be noted, however, that the stress value obtained by HR-EBSD in a given scanning point is the average stress on the area illuminated by the incoming electron beam. As a result, at large enough stress levels, the probability distribution $p(\sigma)$ measured deviates from the inverse cubic decay—it turns to a much faster decaying regime [21]. Nevertheless, for most cases one can easily identify a linear regime on the second-order restricted moment $v_2(\sigma)$ versus $\ln(\sigma)$ plot (see Fig. 4). From the deviation of the inverse cubic decay, we can define a characteristic length scale $r_d = \mu b/\sigma_d$, where σ_d is the stress level where the probability distribution starts to deviate from the inverse cubic regime.

In the investigations performed, $r_d \approx 75$ nm. This means that short-range dislocation structures (such as dipoles) narrower than r_d are not "seen" by this method. So, compared to XPA, HR-EBSD somewhat underestimates the dislocation density (for details see below).

Since from the HR-EBSD analysis one can obtain five independent stress components (σ_{33} is assumed to vanish in the HR-EBSD analysis), a formal dislocation density $\rho_{ij}^* = b^2 \mu^2/(8\pi)C_{ij}\langle\rho\rangle$ can be determined from the stress maps corresponding to different ij stress components, where the parameter C_{ij} is the contrast factor of the ijth stress component. Unlike for the x-ray line broadening, there is no existing analytical calculation to give the precise value for C_{ij}. In the theoretical paper on the internal stress distribution [23], C_{ij} is calculated only for the shear stress generated by edge dislocations in isotropic materials in the coordinate system defined by the Burgers and line direction vectors of the dislocations. In this specific case, $C_{\text{shear}} = \pi/[2(1-\nu)^2)]$, where ν is the Poisson's ratio. According to our experimental results for the case studied in the paper, C_{ij} varies significantly (by a factor of about 5). In the results presented below, we give only the average of the five formal dislocation densities normalized by C_{shear}. The issue, however, requires further investigations.

A typical stress map, stress probability distribution, and the corresponding second-order restricted moment can be seen in Fig. 4.

TEM investigations

A TEM specimen was fabricated from the bulk copper single crystal deformed up to 43.12 MPa resolved shear stress with the aim of qualitative comparison of dislocation structures with those obtained from GND density maps. The TEM lamella preparation was carried out using a FEI Quanta 3D FEG dual-beam SEM-FIB microscope. The initial fabrication process was carried out at 30 kV acceleration voltage and ion currents of 1–30 nA. The final polishing consisted of low current (0.2−0.5 nA) and low voltage (2−5 kV) ion polishing. It is noted that to be able to investigate very large dislocation cells unusually large (20 μm × 20 μm) specimens were fabricated requiring extra care during the preparation process [26–28]. Bright field images of the dislocation network were recorded on a $6 \times 6\,\text{cm}^2$ 4k × 4k CETA 16 CMOS camera with 14 μm pixel size, controlled by VELOX software in a Titan Themis G2 200 transmission electron microscope operated at 200 kV (see Fig. 13).

IV. FRACTAL ANALYSIS

The dislocation cell structure developing under unidirectional deformation at ideal multiple slip is known to be a so-called hole fractal [9] consisting of connected walls and cell interiors with a power-law-type size distribution. Since the GND maps obtained by HR-EBSD measurements allow us to study the dislocation microstructure on a much larger area than one can do with TEM (applied traditionally for microstructure characterization), we performed fractal dimension analysis on the GND maps at different stress levels.

We have applied two different methods, the traditional box counting and the correlation dimension analysis.

A. Box-counting algorithm

A common algorithm to determine the fractal dimension of a set is the well-known box-counting algorithm [29]. In the method, we cover the image with an equidistant grid of lattice spacing L, and then count the number of boxes N containing GNDs above a threshold level (for details, see below). The fractal dimension D_H is

$$D_H = \frac{d\ln(N)}{d\ln(L)}, \tag{11}$$

that is obtained by fitting a straight line to the $\ln(N)$ versus $\ln(L)$ plot. (D_H is often referred to as Hausdorff dimension.) The advantage of the method is that it is numerically a cheap, fast, and fairly precise procedure.

B. Correlation dimension

One can also measure the geometrical randomness of points through the so-called correlation integral, which may be estimated for large enough systems with the correlation sum [30]

$$C(\epsilon) = \frac{1}{N(N-1)} \sum_{i \neq j}^{N} H(\epsilon - |r_i - r_j|), \tag{12}$$

where ϵ is the threshold distance, N is the number of nonzero points, H is the Heaviside step function, r_i and r_j are the coordinates of the set points. The correlation integral scales with the threshold distance as [30]

$$C(\epsilon) \propto \epsilon^{D_c}, \tag{13}$$

where D_c is the correlation dimension. One can easily see that for points on a circle, the correlation dimension $D_c = 1$, for points on a sphere $D_c = 2$ and for points evenly distributed in a sphere $D_c = 3$. For the analysis of 2D embedded geometrical structures, one may expect that $1 \leqslant D_c \leqslant 2$.

C. Image filtering

The GND maps measured cannot be analyzed with the method explained above in a straightforward manner. One issue is that the maps are obviously not binary ones so, one has to introduce some threshold value above which we consider the map intensity to be 1 and 0 below. The fractal dimension obtained may depend on the threshold value chosen. Another problem we face is that the GND map contains numerous random points. They may correspond to individual dislocations or narrow dislocation multipoles but certainly they should not be considered during the fractal analysis.

A simple method for global binarization is the so-called Otsu's method [31,32]. (It is analogous to Fisher's discriminant analysis [33] method and equivalent to a globally optimized k-means clustering method [34,35].) In the simplest form, it returns a binarized intensity map threshold by maximizing the interclass variance. To get this threshold value, first the probability distribution of the point intensity $p(I)$ is calculated numerically with some appropriate binning level
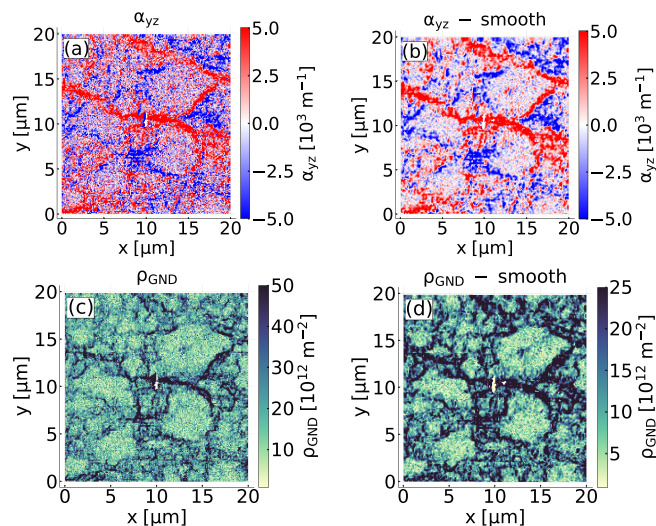
FIG. 5. Example for α_{yz} maps and GND density maps obtained with and without smoothing for the sample compressed up to 43.12 MPa. (a) α_{yz} map without smoothing, (b) with smoothing, (c) GND map without smoothing, (d) with smoothing.

FIG. 6. (a) Otsu's binarization method with box size of 1 μm, (b) 5 μm, (c) the added binary maps at all binarization sizes, and (d) the map after the final binarization.

chosen. After this, with a threshold level t the histogram $p(I)$ is cut into two subhistograms separated by the threshold, and the quantity

$$\sigma_w^2(t) = P_0(t)\sigma_0^2(t) + P_1(t)\sigma_1^2(t) \tag{14}$$

is calculated, where P_0 and P_1 are the probabilities of the two classes separated by t, while σ_0^2 and σ_1^2 are variances of the two classes. The threshold for the image binarization is selected by minimizing $\sigma_w(t)$.

Otsu's method performs exceptionally well when the histogram obtained on the image has a bimodal distribution and the background and foreground values are separated by a deep valley. However, if the image is corrupted with additive noise or the variation of intensities between background and foreground are large compared to the mean difference, the histogram may degrade.

One may observe a fluctuating salt-and-pepper-like noise on the raw Nye-tensor component maps and GND density maps (Fig. 5). This prevents the direct applicability of Otsu's method. To eliminate this noise, a smoothing window was applied to the measurable Nye-tensor components. The maps were convoluted with a circular averaging window of radius $r = 150$ nm. The application of a smoothing window results in a more pronounced dislocation wall structure (Fig. 5). A globally applied binarization method discussed above may ignore those dislocation walls, which may have a lower dislocation density than the thickest dislocation ensembles. To avoid this problem a multiscale binarization method was developed. The area map was subdivided into squared subareas and Otsu's method was applied separately for each subarea (Fig. 6). By repeating this algorithm with areas with different sizes and by adding up the maps binarized with different scales we could obtain a purely bimodal histogram for the image (Fig. 6). The effect of the method for the intensity histograms is seen in Fig. 7. After the multiscale binarization method explained above, the histogram is clearly bimodal
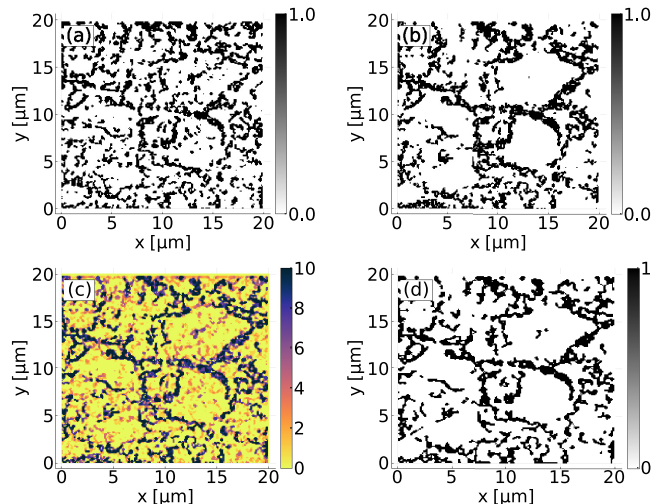
allowing to define a threshold level. Those pixels were considered as dislocation walls which had a higher value than the intensity value corresponding to the minimum of the histogram valley. This method is a powerful tool to obtain not only the global but also the globally invisible, locally present dislocation walls (see Fig. 6).
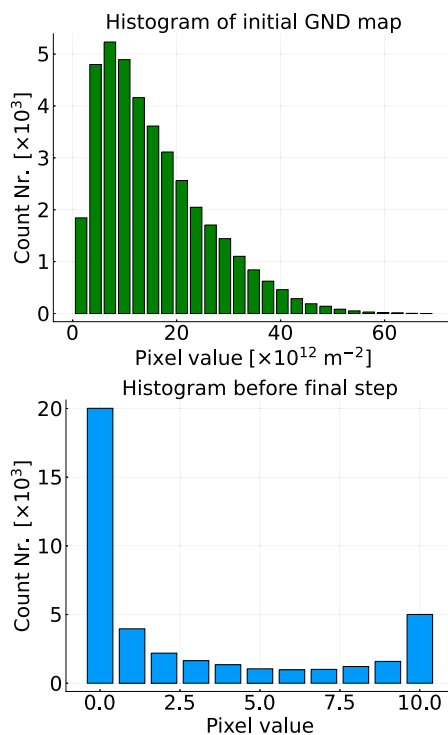

FIG. 7. The histogram before (upper box) and after (lower box) image filtering.

D. Burgers vector analysis

As discussed above, only the α_{iz}, $i = x, y, z$; components of the Nye tensor can be determined from a HR-EBSD measurement without any further assumption regarding the dislocation system (Fig. 13). Therefore, according to Eq. (8) the vector constructed from the available Nye-tensor components

$$\vec{B} = (\alpha_{xz}, \alpha_{yz}, \alpha_{zz}) \qquad (15)$$

is

$$B_i = \sum_t b_i^t \rho^t \cos(\vartheta^t), \qquad (16)$$

where ϑ^t is the angle between the line direction of the tth type dislocation and the surface normal vector. To characterize the type and sign of the dislocation at a given point of the scanned surface the method introduced in Ref. [36] is followed, that is, the quantity

$$a_i = \cos(\varphi_i) = \frac{\vec{B} \cdot \vec{b}_i}{B b_i} \qquad (17)$$

can be calculated where the index i goes through all the six Burgers vectors existing in the FCC crystal [36]. Certainly, one cannot determine the relative population of the different types of dislocations from $\vec{B}$, but according to the definition given by Eq. (17) if the ρ^t density of one of the Burgers vectors is dominantly larger than the other ones, the absolute values of the corresponding a_i are close to 1. Therefore, a_i values can help to describe the type of dislocations at the sample surface. To visualize this, the product of the a_i value and the local GND density was calculated at each measurement point and plotted for the six possible Burgers vectors. (Typical results can be seen in Fig. 16.)

V. RESULTS AND DISCUSSION

As a first step, x-ray line profile measurements with {020} Bragg reflection were performed on the (010) surface of the six samples deformed up to different stress levels. According to earlier investigations on deformed Cu single crystals oriented for ideal multiple slip [17] for this reflection $\Lambda = 0.783$. The intensity distributions were analyzed with the restricted moment method explained earlier. Both the second- and the fourth-order restricted moments were evaluated.

As can be seen in Fig. 8, the Taylor linear relation between the square root of the dislocation density and the resolved shear stress is fulfilled. A relatively small deviation can be seen at lowest $\tau^* = 17.43$ MPa stress level. They are definitely larger then the accuracy of the determination of formal dislocation density. The deviations can be attributed to the fact that for the small deformation level in stage II, the dislocation population may differ from the one obtained in the investigations presented in Ref. [17]. As a consequence, the contrast factor can be somewhat different from the one used. The results are in agreement with the earlier investigations of Székely *et al.* [11]. However, as mentioned earlier, the x-ray detector used in the measurements reported here has a much better signal-to-noise ratio than the one used earlier, resulting in a much more improved accuracy of the current study.
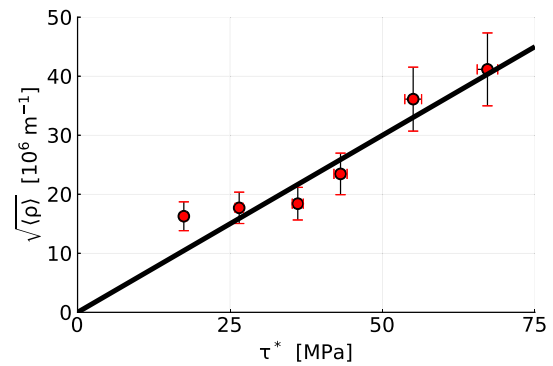

FIG. 8. The $\sqrt{\langle \rho \rangle} - \tau^*$ relation, where $\langle \rho \rangle$ is the average dislocation density measured by x ray and τ^* is the resolved shear stress.

In Fig. 9, the $v^4(q)/q^2$ restricted moments are plotted for the undeformed and the six deformed samples. It can be seen even without any curve fitting that the asymptotic part of the curves tend to a constant value that increases monotonically with the applied stress. Since the asymptotic value of the $v^4(q)/q^2$ is proportional to the average dislocation density this is in accordance with the results discussed above. It is remarkable, however, that the maximum values of the curves normalized with the asymptotic value are not monotonous with the stress. It has a clear maximum at 36.11 MPa stress level. After performing the fitting of the function given by Eq. (4), the σ value defined by Eq. (5) can be determined.

In agreement with the phenomenological feature mentioned above, the σ versus τ curve exhibits a sharp maximum at $\tau = 36.11$ MPa (see Fig. 10) corresponding to the stage II to stage III transition stress level (see Fig. 1). (For the undeformed sample, it is assumed that the dislocation network is nearly homogeneous, so the fluctuation is zero.) The results obtained are in agreement with the ones reported earlier on the same material [11].

As suggested earlier by Mughrabi and coworkers [37,38], the dislocation system can be envisaged as a composite of hard dislocation walls with dislocation density of ρ_w and soft cell
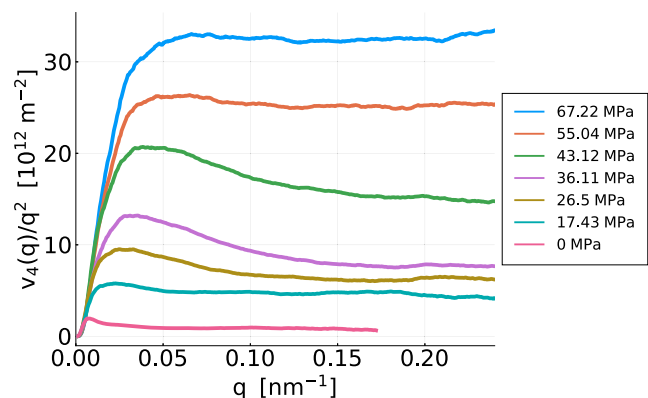

FIG. 9. The $v^4(q)/q^2$ versus q curves at different compression levels. The corresponding resolved shear stresses are indicated in the upper right corner.
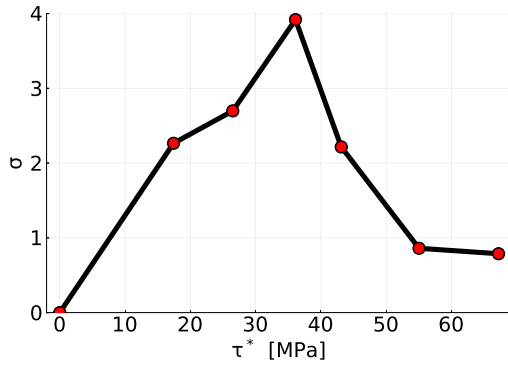
FIG. 10. The $\sigma(\tau^*)$ function is represented, where σ is the average dislocation density fluctuation.
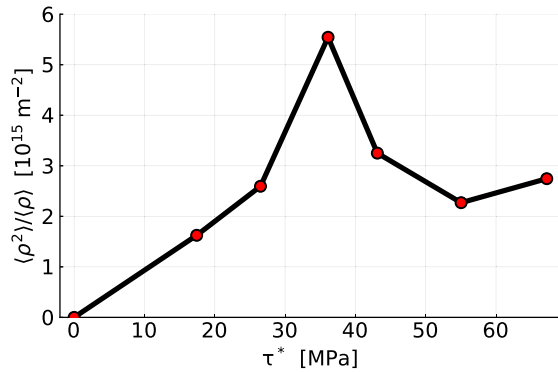

FIG. 11. The apparent dislocation density ρ_w^{app} as a function of the resolved shear stress.
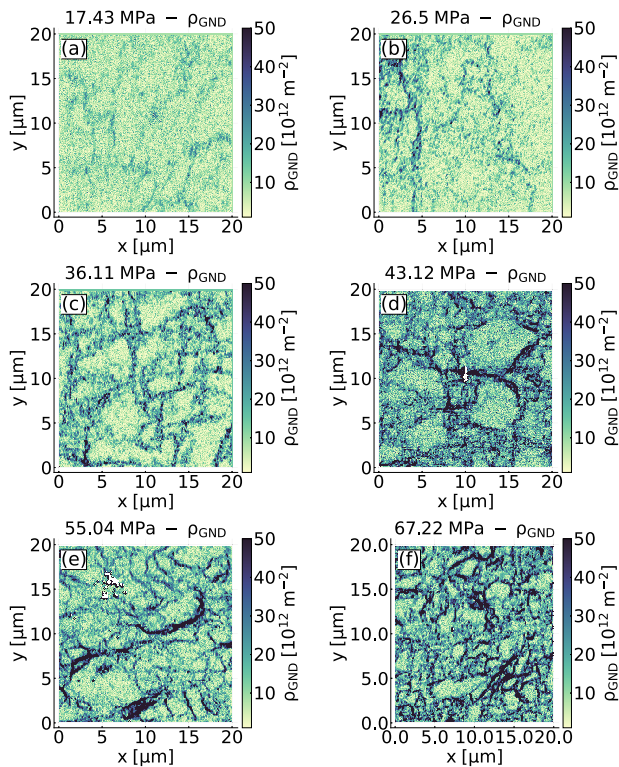

FIG. 12. The GND density maps obtained on samples deformed up to (a) 17.43, (b) 26.5, (c) 36.11, (d) 43.12, (e) 55.04, and (f) 67.22 MPa.
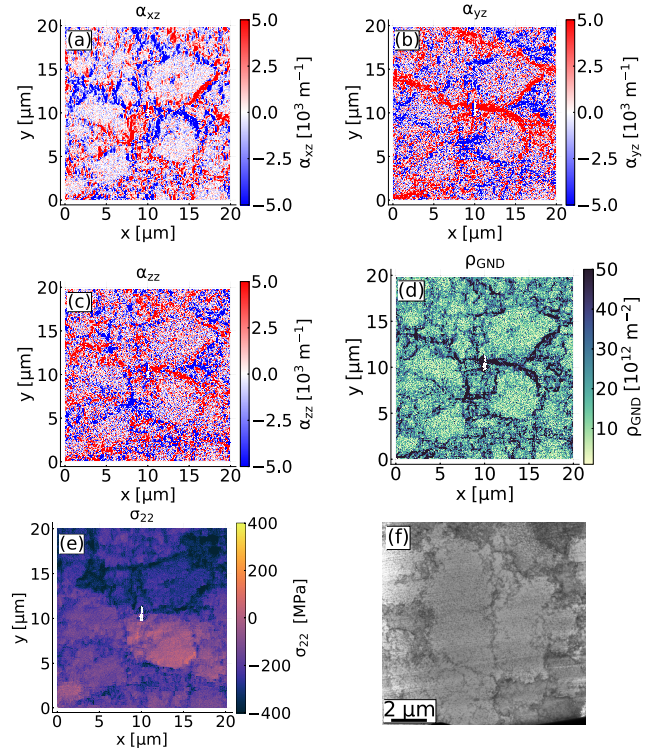

FIG. 13. Maps of the (a) α_{13}, (b) α_{23}, and (c) α_{33} components, (d) the GND, the (e) σ_{22}, and (f) a TEM picture obtained on the sample deformed up to 43.12 MPa. Notice that the scale and the observation site on the TEM picture is different than on the other ones.

interiors with dislocation density ρ_c. Within this model,

$$\langle \rho \rangle = f\rho_w + (1-f)\rho_c \tag{18}$$

and

$$\langle \rho^2 \rangle = f\rho_w^2 + (1-f)\rho_c^2, \tag{19}$$

where f is the volume fraction of the cell walls. Since according to earlier investigations [37,38], f is in the order of 0.1, and ρ_w is an order of magnitude higher than ρ_c, the second term in $\langle \rho^2 \rangle$ can be neglected so

$$\langle \rho^2 \rangle \approx f\rho_w^2. \tag{20}$$

With this, the quantity $\rho_w^{\mathrm{app}} = \langle \rho^2 \rangle / \langle \rho \rangle$, that can be determined directly from the x-ray line profile, is

$$\rho_w^{\mathrm{app}} = \rho_w \frac{1}{1 + \frac{(1-f)\rho_c}{f\rho_w}}. \tag{21}$$

If the dislocation content in the cell interiors is much smaller than in the cell walls, i.e., $(1-f)\rho_c \ll f\rho_w$ then the apparent dislocation density $\rho_w^{\mathrm{app}} \approx \rho_w$. According to Fig. 11 in stage II, ρ_w^{app} increases monotonically and at the stage II to III transition stress level it has a maximum. In stage III, at large enough stress it tends to saturate.

Based on the x-ray line profile results, it can be concluded that during stage II the dislocation distribution becomes more and more inhomogeneous, dense dislocation walls are formed with an increasing ρ_w dislocation density. At a given deformation level, however, the dislocation density in the walls
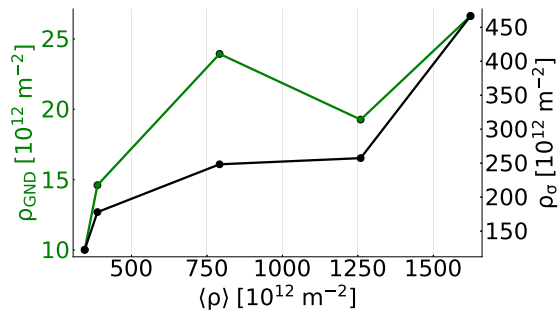
FIG. 14. The dislocation densities obtained from the stress probability distribution (black curve) and from the Nye's tensor components (green curve) versus the dislocation density obtained by x-ray line profile analysis.

reaches a maximum level, dislocation annihilation prevents the further increase of the dislocation density. This process is called dynamic recovery [37]. In stage III, new walls and an increase of the dislocation density in the cell interiors is needed to accumulate more dislocations. According to Fig. 11, for large enough stress levels the term $(1 - f)\rho_c/f/\rho_w$ is in the order of unity (ρ_{app} droops down to about the half of its maximum value).

As seen above, XPA is a rather powerful method to determine some average statistical properties of the dislocation microstructure but certainly it is not able to say anything about the actual dislocation morphology.

Besides the traditionally applied TEM [39], the relatively recently developed HR-EBSD method offers another perspective to directly study the dislocation microstructure. A big advantage of the HR-EBSD is that a much larger area can be studied than by TEM. Moreover, the sample preparation is much easier. Figure 12 shows the GND maps obtained on the six deformed samples. At each deformation level, a clear cell structure can be seen with increasing volume fraction of the cell walls. In Fig. 13, the maps of the three α_{iz} components, the GND density, the stress component σ_{yy}, and a TEM picture obtained on the sample deformed are plotted. Similar pictures were obtained for the other stress levels studied.

According to Fig. 13, as assumed earlier [37,38], long-range internal stresses develop in the cell interiors. Unlike XPA, HR-EBSD is a direct method to determine the local stress state of the sample, so the result obtained is direct evidence of the presence of long-range internal stresses.

The dislocation density was also determined from the stress maps by the restricted moment analysis of the internal stress distribution. To reduce the error, the average of the ρ_{ij}^* values were calculated for the five independent components of the stress tensor. The results obtained are plotted in Fig. 14. As seen, there is correlation between the ρ_σ average dislocation density obtained from the stress maps and the $\langle\rho\rangle$ density found by the XPA, but the relation is clearly not linear. One can also note that in some points (for example, in the fourth), a higher difference is present. This is probably due to the local nature of the HR-EBSD but also due to the fact that the measurements were carried out on different samples, not on the same surface and place. Moreover, the C_{ij} geometrical factor may vary with stress and due to the finite volume
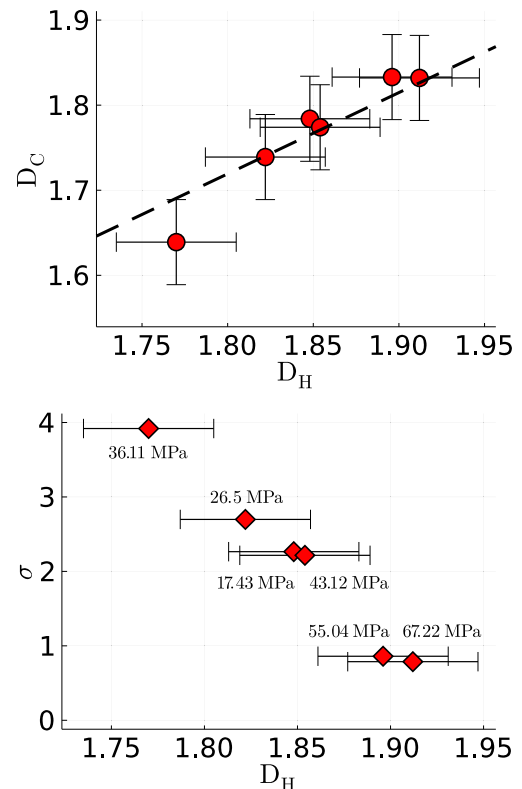

FIG. 15. In the upper image, the correlation dimension D_c is presented versus the Hausdorff-dimension D_H obtained by box counting. In the down figure, the average dislocation density fluctuation is shown in function of the Hausdorff-dimension.

illuminated by the electrons, we cannot detect the small dislocation dipoles (see above). So, the HR-EBSD internal stress analysis is a possible method for the determination of the dislocation density, but the issue requires further investigation to be able to produce dislocation density values with high precision.

The average GND density ρ_{GND} defined by Eq. (9) was also determined from the Nye's tensor maps. According to Fig. 14, as a general trend ρ_{GND} increases with increasing deformation, but due to the large dislocation density fluctuation, to get more precise GND density values, one should perform EBSD measurements on a very large area that was not possible with the setup used.

After the image binarization with the method explained above, the fractal dimensions of the ρ_{GND} maps plotted in Fig. 12 were also determined by both the box-counting (D_H) and correlation dimension (D_c) analysis. The results obtained are plotted in Fig. 15. It is found that $D_c \approx 0.95 D_H$, so the two methods give the same fractal dimension within experimental error. This consistent correlation confirms the formation of a special dislocation structure with noninteger (fractal) dimension. It is, however, a nontrivial and somewhat unexpected result that the fractal dimension is decreasing with increasing relative dislocation density fluctuation σ. In other words, in the stage II deformation regime, the fractal dimension decreases with increasing stress level but it starts to increase in stage III. So, like the relative dislocation density fluctuation, the fractal dimension also has an extremum value at the stage
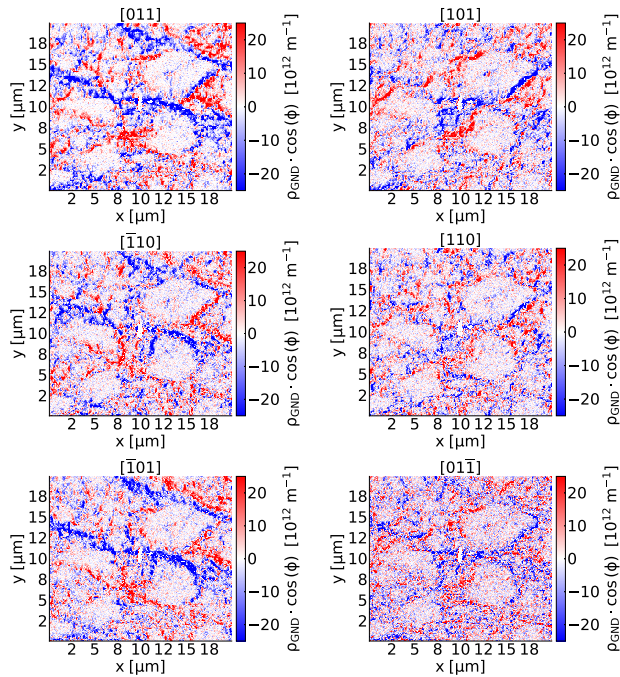
FIG. 16. The $\rho_{\text{GND}} \cdot a_i$, $i = 1...6$ maps obtained on the sample compressed up to 43.12 MPa.

II to III transition. This means that the factal dimension is not controlled directly by the average dislocation density but the relative dislocation density fluctuation. This behavior has a rather important implication for the general form of the theory of dislocation patterning. A proper theory should predict the dislocation density fluctuation, not only the average dislocation density. In Sec. IV D, a method was outlined to analyze Burgers vectors based on the projection of vector $\vec{B}$ to the different possible Burgers vectors [36]. For the sample deformed up to 43.12 MPa the different $\rho_{\text{GND}} \cdot a_i$ maps obtained are plotted in Fig. 16. Similar behavior is found for the other samples. As seen, some of the walls have a positive (red) or negative (blue) net Burgers vector while the other ones are more dipole like with a positive net Burgers vector on one side and a negative one on the other side.

This picture somewhat refines the composite model proposed by Mughrabi *et al.* [37,38]. In the original form of the model, the sources of the long-range stress are the two dislocation walls allocated on the two sides of a cell wall. The dislocation walls are formed by the reaction of dislocations in two slip systems, resulting in a Burgers vector parallel to the surface of the cell wall, i.e., the GND structure imagined is dipolelike. However, an elongated region with finite length d having a net Burgers vector can also generate long-range

internal stress within the connected $d \times d$ sized area. So, the sources of the long-range stresses are not necessary dipolelike walls as assumed earlier.

VI. SUMMARY AND CONCLUSIONS

Copper single crystals oriented for (100) ideal multiple slips were compressed uniaxially up to different stress levels. The dislocation microstructures developing in the samples were studied by XPA and HR-EBSD.

The main conclusions are:

(1) It is shown that HR-EBSD offers an efficient method to study dislocation microstructures with much less sample preparation effort than TEM conventionally applied.

(2) The presence of the long-range internal stress developing in the cell interiors is directly seen by HR-EBSD measurements. Moreover, the stress maps can be directly measured.

(3) Some of the walls have a positive or negative net Burgers vector while the other ones are more dipolelike with positive net Burgers vector on one side and negative one the other side;

(4) According to x-ray line profile investigations on compressed Cu single oriented for ideal multiple slips, the relative dislocation density fluctuation exhibits a sharp maximum at stage II to III transition stress level;

(5) The most important finding of the investigations is that the dislocation cell structure is well described by a hole fractal with fractal dimension decreasing monotonically with the relative dislocation density fluctuation. So, it is directly controlled by the level of fluctuations developing in the system.

The results obtained can be directly compared to the prediction of the theoretical models, so they can help to inspire and validate them. Finally, it is important to emphasize that there are still a lot of issues that should be addressed. One very important question is related to size effect, especially the formation of cells in micropillars, that may lead to unique interesting results. Moreover, it would be important to study *in situ* the cell formation process.

[1] N. Hansen and D. Kuhlmann-Wilsdorf, Low energy dislocation structures due to unidirectional deformation at low temperatures, Mater. Sci. Eng. **81**, 141 (1986).

[2] D. L. Holt, Dislocation cell formation in metals, J. Appl. Phys. **41**, 3197 (1970).

[3] J. Rickman and J. Vinals, Modelling of dislocation structures in materials, Philos. Mag. A **75**, 1251 (1997).

[4] D. Walgraef and E. C. Aifantis, Dislocation patterning in fatigued metals as a result of dynamical instabilities, J. Appl. Phys. **58**, 688 (1985).

[5] J. Pontès, D. Walgraef, and E. Aifantis, On dislocation patterning: Multiple slip effects in the rate equation approach, Int. J. Plast. **22**, 1486 (2006).

[6] I. Groma, M. Zaiser, and P. Ispánovity, Dislocation patterning in a two-dimensional continuum theory of dislocations, Phys. Rev. B **93**, 214110 (2016).

[7] R. Wu, D. Tüzes, P. D. Ispánovity, I. Groma, T. Hochrainer, and M. Zaiser, Instability of dislocation fluxes in a single slip: Deterministic and stochastic models of dislocation patterning, Phys. Rev. B **98**, 054110 (2018).

[8] R. Wu and M. Zaiser, Cell structure formation in a two-dimensional density-based dislocation dynamics model, Mater. Theory **5**, 1 (2021).

[9] P. Hähner, K. Bay, and M. Zaiser, Fractal Dislocation Patterning During Plastic Deformation, Phys. Rev. Lett. **81**, 2470 (1998).

[10] M. Zaiser and P. Hähner, The flow stress of fractal dislocation arrangements, Mater. Sci. Eng.: A **270**, 299 (1999).

[11] F. Szekely, I. Groma, and J. Lendvai, Statistic properties of dislocation structures investigated by x-ray diffraction, Mater. Sci. Eng.: A **309**, 352 (2001).

[12] B. Bakó and W. Hoffelner, Cellular dislocation patterning during plastic deformation, Phys. Rev. B **76**, 214108 (2007).

[13] P. Hähner and M. Zaiser, Dislocation dynamics and work hardening of fractal dislocation cell structures, Mater. Sci. Eng.: A **272**, 443 (1999).

[14] A. D. Rollett and F. Kocks, A review of the stages of work hardening, in *Dislocations '93*, Solid State Phenomena (Trans Tech Publications Ltd, 1993), Vol. 35, pp. 1–18.

[15] I. Groma, X-ray line broadening due to an inhomogeneous dislocation distribution, Phys. Rev. B **57**, 7535 (1998).

[16] I. Groma, T. Ungár, and M. Wilkens, Asymmetric x-ray line broadening of plastically deformed crystals. I. Theory, J. Appl. Crystallogr. **21**, 47 (1988).

[17] T. Ungár, I. Groma, and M. Wilkens, Asymmetric x-ray line broadening of plastically deformed crystals. II. Evaluation procedure and application to [001]-Cu crystals, J. Appl. Crystallogr. **22**, 26 (1989).

[18] T. B. Britton and A. J. Wilkinson, High resolution electron backscatter diffraction measurements of elastic strain variations in the presence of larger lattice rotations, Ultramicroscopy **114**, 82 (2012).

[19] E. Kröner, Continuum theory of defects, Phys. Defects **35**, 217 (1981).

[20] W. Pantleon, Resolving the geometrically necessary dislocation content by conventional electron backscattering diffraction, Scr. Mater. **58**, 994 (2008).

[21] S. Kalácska, I. Groma, A. Borbély, and P. D. Ispánovity, Comparison of the dislocation density obtained by HR-EBSD and x-Ray profile analysis, Appl. Phys. Lett. **110**, 091912 (2017).

[22] S. Kalácska, Z. Dankházi, G. Zilahi, X. Maeder, J. Michler, P. D. Ispánovity, and I. Groma, Investigation of geometrically necessary dislocation structures in compressed Cu micropillars by 3-dimensional HR-EBSD, Mater. Sci. Eng.: A **770**, 138499 (2020).

[23] I. Groma and B. Bakó, Probability distribution of internal stresses in parallel straight dislocation systems, Phys. Rev. B **58**, 2969 (1998).

[24] F. F. Csikor and István Groma, Probability distribution of internal stress in relaxed dislocation systems, Phys. Rev. B **70**, 064106 (2004).

[25] D. Wallis, L. N. Hansen, A. J. Wilkinson, and R. A. Lebensohn, Dislocation interactions in olivine control postseismic creep of the upper mantle, Nat. Commun. **12**, 3496 (2021).

[26] J. Mayer, L. A. Giannuzzi, T. Kamino, and J. Michael, TEM sample preparation and FIB-induced damage, MRS Bull. **32**, 400 (2007).

[27] L. A. Giannuzzi and F. A. Stevie, *Introduction to Focused Ion Beams: Instrumentation, Theory, Techniques and Practice* (Springer Science & Business Media, New York, 2004).

[28] N. Yao, *Focused Ion Beam Systems: Basics and Applications* (Cambridge University Press, Cambridge, 2007).

[29] H. Salat, R. Murcio, and E. Arcaute, Multifractal methodology, Physica A **473**, 467 (2017).

[30] P. Grassberger and I. Procaccia, Measuring the strangeness of strange attractors, in *The Theory of Chaotic Attractors* (Springer, New York, 2004), pp. 170.

[31] N. Otsu, A threshold selection method from gray-level histograms, IEEE Trans. Syst. Man Cybern. **9**, 62 (1979).

[32] S. U. k. Lee, S. Y. Chung, and R. H. Park, A comparative performance study of several global thresholding techniques for segmentation, Comput. Vision, Graphics Image Process. **52**, 171 (1990).

[33] R. A. Fisher, The use of multiple measurements in taxonomic problems, Ann. Eugen. **7**, 179 (1936).

[34] J. MacQueen, Some methods for classification and analysis of multivariate observations, in *Proceedings of the Fifth Berkeley Symposium on Mathematical Statistics and Probability* (University of California Press, Oakland, CA, 1967), Vol. 114, pp. 281–297.

[35] H.-P. Kriegel, E. Schubert, and A. Zimek, The (black) art of runtime evaluation: Are we comparing algorithms or implementations? Knowl. Inform. Syst. **52**, 341 (2017).

[36] K. Zoller, S. Kalácska, P. D. Ispánovity, and K. Schulz, Microstructure evolution of compressed micropillars investigated by *in situ* HR-EBSD analysis and dislocation density simulations, Comptes Rendus. Physique **22**, 267 (2021)

[37] H. Mughrabi and T. Ungár, Long-range internal stresses in deformed single-phase materials: The composite model and its consequences, in *Dislocations in Solids*, (Elsevier, Amsterdam, The Netherlands, 2002), Vol. 11 pp. 343–411.

[38] T. Ungar, H. Mughrabi, D. Rönnpagel, and M. Wilkens, X-ray line-broadening study of the dislocation cell structure in deformed [001]-orientated copper single crystals, Acta Metall. **32**, 333 (1984).

[39] A. Oudriss and X. Feaugas, Length scales and scaling laws for dislocation cells developed during monotonic deformation of (001) nickel single crystal, Int. J. Plast. **78**, 187 (2016).